Extreme Mechanics Letters 48 (2021) 101397

Contents lists available at ScienceDirect

Extreme Mechanics Letters

journal homepage: www.elsevier.com/locate/eml

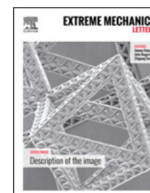

In situ characterization of buckling dynamics in silicon microribbon on an elastomer substrate

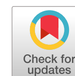

Zhuohui Zeng [a,b], Hongyu Yu [a], Xian Chen [a,*]

[a] Department of Mechanical and Aerospace Engineering, Hong Kong University of Science and Technology, Hong Kong
[b] Greater Bay Joint Division, Shenyang National Laboratory for Materials Science, Tat Chee Avenue, Hong Kong

ARTICLE INFO

Article history:
Received 18 May 2021
Received in revised form 11 June 2021
Accepted 11 June 2021
Available online 19 June 2021

Keywords:
Stretchable electronics
Thin film buckling
Differential interference microscope
Buckling dynamics

ABSTRACT

Buckling of rigid thin films on elastomer substrates underlies the fabrication foundation of stretchable soft electronics. Here we demonstrate an optical approach to in situ characterize the buckling of silicon microribbon driven by releasing the pre-stretched poly-dimethylsiloxane (PDMS) substrate at a controllable strain rate. The method, based on quantitative differential interference microscopy, directly captures the space–time evolution of the surface topography at a frame rate of 100 fps in a large field of view of $50 \times 195\ \mu m^2$. The nucleation, propagation and stabilization of the buckled structure during the buckling and unbuckling processes are observed and quantified. Our experiment reveals that a sequence of partially buckled patterns are energetically stable to bridge the unbuckled and fully buckled states. This work opens a new experimental scheme for the research on stretchable soft electronics and provides new evidence for the theoretical study of the buckling dynamics.
© 2021 Elsevier Ltd. All rights reserved.

1. Introduction

Micro-electro-mechanical systems (MEMS) play a profound role in semiconductor and electronics industry for its wide applications in micro devices such as strain sensors [1–3], actuators [4, 5] and microrobotics [6]. The precision of structural design and the deformability of the fabricated structure are critical to the functionality and stability of MEMS devices, especially microrobotics [7,8] and biomedical devices [9,10]. Such demand on precise structural formation arises dramatically in emerging foldable and stretchable soft electronics [8,11,12]. While there are many methods to fabricate various delicate MEMS structures [11, 12], the quantitative characterization of the structure and deformation of these micro devices is rare. Understanding how the thin film structure deforms and propagates on the soft substrate under various loading rates is not only essential for the development and design of flexible electronics, but also governs the deployment and usage of these devices in practice. By far, atomic force microscopy (AFM) has been nearly the sole actor on this stage [13–22]. As a scanning-based probe, one can conduct the surface scans while holding and tuning the load step by step to obtain the evolution of surface structures, but AFM cannot measure how the flat micro-layers deform to their 3D functional structures at different strain rates. Some time-resolved attempts were made using optical microscope and fast scanning electron microscopy (SEM) under mechanical loading [23,24]. But those methods cannot quantitatively resolve the topographic evolution. If the surface deformation is highly periodic, then the topography evolution can be quantified from the scattering between light and periodic structures by the optical interferometer [25]. But when the structure is very non-periodic, the intensity would be too weak for an accurate structural reconstruction. From this point of view, an in situ structural characterization in sub-micron to millimeter length scale is urgently needed.

A recent advance in quantitative optics for full-field deformation characterization [26,27] sheds light on in situ structural characterization for MEMS. This method, based on differential interference contrast microscope (DInM), characterizes a large field of view in milliseconds, which breaks the bottleneck of the scanning-based probes for in situ experiments. The topographical gradient of surface can be analytically derived from the light path difference between two orthogonally polarized beams. Based on the localization analysis of light, the beam-shear angles can be precisely characterized [28], through which sub-micron surface structural features can be resolved by highly coherent blue LED light source [27]. Utilizing the programmable phase tuning by liquid crystal retarders and algorithmically cooperating digital image correlation, a dual beam-shear differential interference microscope (i.e. D-DInM) was designed and built for in situ characterization of deformation processes in a crystalline solid undergoing stress-induced phase transformation [27]. In this letter, we utilize the same D-DInM system with beam-shear vector $(s_1, s_2) = (588, 591)$ nm to study the dynamics of silicon (Si) microribbon buckling on a polydimethylsiloxane (PDMS)

* Corresponding author.
E-mail address: xianchen@ust.hk (X. Chen).

https://doi.org/10.1016/j.eml.2021.101397
2352-4316/© 2021 Elsevier Ltd. All rights reserved.

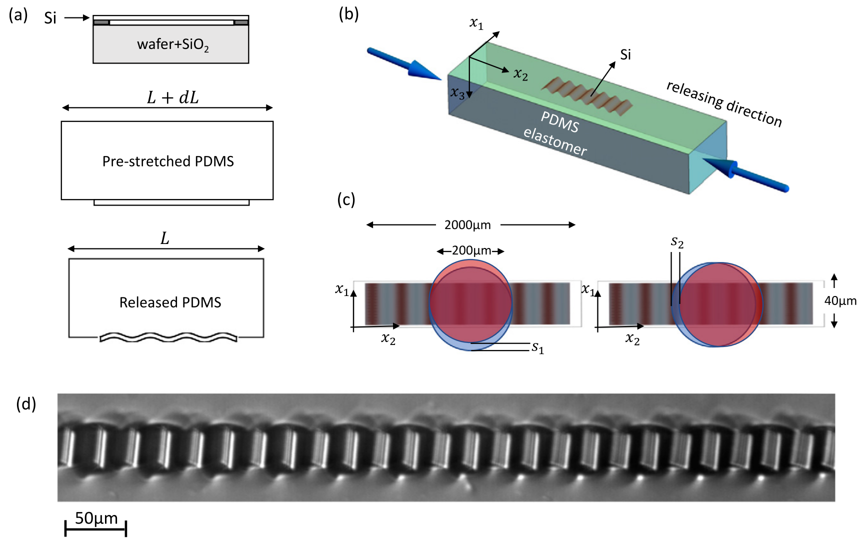

Fig. 1. (a) The fabrication process of Si microribbon on PDMS elastomer substrate. (b) Schematics of uniaxial loading setup for a buckled Si microribbion upon releasing the PDMS elastomer. (c) Optics dual beam-shear configuration of the D-DInM. The blue and red circles denote the polarized light beams that are spatially sheared along x_1-axis by s_1 in BS1 mode and along x_2-axis by s_2 in BS2 mode. (d) The buckled Si microribbon on PDMS captured by the D-DInM system.

substrate. For the dynamic measurement, we switched off one of the beam-shear modes to achieve sufficiently high frame rate such that the time-dependent structural parameters along the loading direction can be quantified during pre-buckling, buckling and post-buckling processes.

2. Optical and mechanical setup for thin film buckling experiment

A free-standing Si thin film with dimension $2000 \times 40 \times 0.35\ \mu\text{m}^3$ was fabricated on a Si/SiO_2 (Silicon-On-Insulator) wafer, shown in the top of Fig. 1(a). Similar to the manufacturing process introduced in Ref. [20], a thin layer of polycrystalline silicon with thickness 350 nm was deposited on the Si/SiO_2 substrate by low-pressure chemical vapor deposition (ASM LB45 LPCVD Furnace). Then we conducted photolithography to pattern a rectangular photoresist ribbon of $2000 \times 40\ \mu\text{m}^2$. Finally, we use buffered oxide etch solution to wash away the unmasked part and the part beneath the Si ribbon. We use a prestretched PDMS elastomer to transfer the Si microribbon from the wafer substrate, shown in the middle of Fig. 1(a). Upon releasing, the thin and long microribbon develops buckling pattern as shown in the bottom of Fig. 1(a). The Si microribbon is strongly adhesive to the PDMS via a UV assisted transfer process [29]. After transferring, the PDMS is released gradually, and a sinusoidal wavy structure is deployed in the Si microribbon, as shown in Fig. 1(d). We do not observe any fractures, nor debonding between Si and the PDMS substrate.

The stretchable PDMS is mounted to a custom uniaxial loading cell so that its releasing/stretching direction is aligned with the longitudinal direction of the Si microribbon, in Fig. 1(b)–(c). The optical probe of differential interference microscopy is set so that the longitudinal direction of the Si microribbon aligns with one of the beam-shear axes (x_2 axis), while the transverse direction naturally aligns with another beam-shear axis (x_1 axis) orthogonal to x_2. The axial loading cell stretches and contracts the PDMS to drive the buckling deformation in Si microribbon under a displacement control.

The spatial topographic gradient of a surface ($\partial x_3/\partial x_1$, $\partial x_3/\partial x_2$) can be analytically calculated from the intensity fields $\hat{\mathcal{I}}_1$ and $\hat{\mathcal{I}}_2$ measured by the differential interference microscope under two different beam-shear modes (BS1 and BS2) [27]. As shown in Fig. 1(c), the light beams with different polarization (*i.e.* the red and blue circles) can be spatially sheared by the D-DInM system in two directions. If they are sheared along x_1 axis by the amount of s_1, we denote it as BS1 mode. If they are sheared along x_2 axis by the amount of s_2, we denote it as BS2 mode. The shear parameters (s_1, s_2) are calibrated independently by the localization analysis [28]. The intensity fields given by the two beam-shear modes are calculated as

$$\text{BS1: } \hat{\mathcal{I}}_1 = \mathcal{I}_0 \sin^2\left(\frac{2\pi s_1}{\lambda}\frac{\partial x_3}{\partial x_1} + \delta_1\right)$$
$$\text{BS2: } \hat{\mathcal{I}}_2 = \mathcal{I}_0 \sin^2\left(\frac{2\pi s_2}{\lambda}\frac{\partial x_3}{\partial x_2} + \delta_2\right) \tag{1}$$

where $\lambda = 460$ nm is the wavelength of the coherent incident light, (δ_1, δ_2) is the programmable phase delays of the optical system for the two beam-shear modes, and the constant $\mathcal{I}_0$ is the reference intensity field that can be calibrated statically at the beginning of the experiment. Direct inverse of functions in (1) gives the surface gradient field ($\partial x_3/\partial x_1$, $\partial x_3/\partial x_2$) in the deformed configuration. After the PDMS substrate is completely released from a 1.5% prestretch, for a $40 \times 250\ \mu\text{m}^2$ surface domain on the Si microribbon (Ω_{DInM}), the gradient distribution along the longitudinal and transverse directions is characterized in Fig. 2(a). The upper and lower bounds of the gradient components are predetermined by the optical parameters. Ref. [27] gives the expression of the range, that

$$\frac{\partial x_3}{\partial x_i} \in \left[\max\left(\frac{-\delta_i}{[s_i]}\right), \min\left(\frac{\pi - \delta_i}{[s_i]}\right)\right], \tag{2}$$

for $i = 1, 2$, and $[s_i] = 2\pi s_i/\lambda$. Substituting the optical parameters of our D-DInM system, we obtain the range of measurement [−0.23, 0.16], within which the trigonometric functions in Eq. (1) are in a monotonic domain. For our experimental setting, this range of measurable gradient components is sufficient for the wavy profile in the Si microribbon. From Fig. 2(a), the gradient component $\partial x_3/\partial x_2$ is highly periodic along x_2 direction, while the gradient component $\partial x_3/\partial x_1$ exhibits a weak periodic effect. In addition, the variation of the $\partial x_3/\partial x_1$ component is much smaller and less regular than that of the $\partial x_3/\partial x_2$ component. The boundary twist of thin ribbon visualized as the oblique blue pattern is clearly revealed by the BS1 mode, while the dominating sinusoidal geometry is captured by the BS2 mode. The inhomogeneous distribution of the transverse $\partial x_3/\partial x_1$ may be

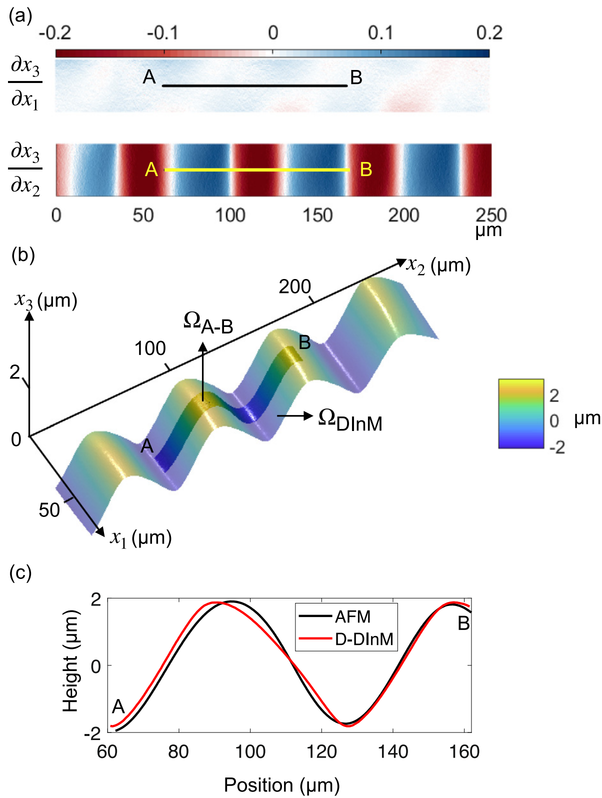

Fig. 2. The static surface topography of the Si microribbon under D-DInM. (a) The gradient fields $\partial x_3/\partial x_1$ and $\partial x_3/\partial x_2$. (b) The reconstructed surface topography and compared with AFM. (c) A detailed comparison between D-DInM and AFM along the segment AB in (a) and (b).

caused by the misalignment between the loading direction and the beam-shear direction of the D-DInM microscope.

Integrating the gradient field over the optical domain Ω_{DInM} gives the 3-dimensional surface topography $x_3(x_1, x_2)$ shown in Fig. 2(b). Within Ω_{DInM}, we select a sub-domain $\Omega_{\text{A-B}}$ to conduct an atomic force microscopy (NanoScope IIIa/Dimension 3100) scan. Comparing the 3-dimensional profiles (Fig. 2(b)) and the 1-dimensional profiles along the segment AB (Fig. 2(c)), the D-DInM optical system provides sufficient precision up to an integration constant. Particularly, the amplitude of the wavy structure is characterized as 1.94 μm by AFM and 2.08 μm by D-DInM corresponding to the wavelength of 66.42 μm by AFM and 64.23 μm by D-DInM for the selected sub-domain $\Omega_{\text{A-B}}$. Given the Young's moduli 2.05 MPa (PDMS) and 160 GPa (Si) and the Poisson ratios 0.48 (PDMS) and 0.27 (Si), the predicted amplitude is 2.34 μm corresponding to the wavelength of 60.29 μm under 1.5% prestrain based on the finite deformation mechanics theory of buckled thin films [20]. Here we show that the static buckling configuration characterized by our D-DInM agrees well with what the continuum theory predicts. Compared to AFM, our quantitative optical method measures the surface topography for a 10 times bigger domain within milliseconds time per frame, which enables a time resolved study of the buckling.

3. Dynamics results and discussion

To demonstrate in situ characterization, we fabricate another Si microribbon with the geometry of 2000 × 40 ×0.3 μm^3 on a PDMS substrate with 2% prestretch. We contract and stretch the PDMS substrate to investigate the evolution of surface topography on the Si microribbon in a 50 × 195 μm^2 field of view. Considering the thin ribbon buckling as a 1-dimensional behavior, we use only the BS2 mode to track the evolution of $\partial x_3/\partial x_2$ as the representation of the time-dependent surface deformation. As a result, a higher data acquisition speed, 100 frames per second, is achieved.

Fig. 3 shows the evolution of centerline gradient during a complete buckling and unbuckling process at different strain rates. The time axis is labeled by the frame number. The strain rate is calculated as $\dot{\ell}/\ell_0$ where $\ell_0 = 15$ mm is the initial length of prestretched PDMS substrate and $\dot{\ell} = d\ell/dt$ is the displacement mobility controlled by a linear actuator (Physik Instrumente MA-35 Micro Actuator) with a maximum displacement mobility of 1 mm/s. In this experiment, we studied the buckling dynamics for a series of strain rates between 0.1 and 5%/s. The size of time windows in the plots is chosen to be inversely proportional to the strain rate. As shown in Fig. 3, an interface between the buckled and the flat structure propagates during the buckling and unbuckling stages under each strain rate. Despite the strain rate, the buckled structures in the Si microribbon are similar with almost the same periodicity of about 49.7 μm. Again, it is comparable to the predicted wavelength of 51.4 μm using the finite deformation mechanics theory of buckled thin films [20]. But the amplitude of gradient peaks varies at different strain rates, and becomes less uniform at higher strain rates, especially for those greater than 3%/s. At all strain rates and in all pairs of neighboring positive and negative gradient peaks in the post-buckling frames, the amplitude of the negative gradient peak (~ -0.24) is larger than that of the positive gradient peak ($\sim$ 0.15), indicating a certain level of asymmetry in the shape of the buckled hills and valleys.

Fig. 4 illustrates the evolution of the centerline gradient during the complete buckling and unbuckling process at the strain rate 0.1%/s by a sequence of snapshots of the centerline gradient profile. Within the field of view, we chase the amplitude and position of the firstly (blue in Fig. 4(a)) and secondly (green in Fig. 4(a)) formed positive gradient peaks to explore the buckling dynamics. Fig. 4(a) shows that the both peaks grow at a nonlinear rate during the formation of the buckled structure. The nonlinear growth curves fit well to an exponential function. Moreover, only the first peak experiences an overshoot, that is the initial value of $\partial x_3/\partial x_2$ is higher than the stabilized value after the thin film fully buckled. It suggests the existence of a barrier of the buckling propagation from the flat state to the fully buckled state. Only when the first peak accumulates sufficient contraction, the whole flat structure loses its stability and bursts to the buckled state. Finally, Fig. 4(c) shows that the two peaks move along two almost parallel spatial trajectories during the whole process, and such trajectories are symmetric between the buckling and unbuckling stages. These phenomena are observed at all strain rates. For the slowest and fastest strain rates, i.e. 0.1%/s and 5%/s, the supplementary movies (S1 and S2) show the time-evolution of 3-dimensional topography during the buckling and unbuckling processes.

We define the buckling speed v as the speed of the peak movement during the buckling stage as shown in Fig. 4(c). Besides, our experiment manifests another characteristic speed, which reveals a longitudinal propagation in the semi-buckled thin film. Here the propagation speed is defined as

$$w = \left| \frac{x_2^{\text{II}} - x_2^{\text{I}}}{t^{\text{II}} - t^{\text{I}}} \right|, \tag{3}$$

where $(t^{\text{I}}, x_2^{\text{I}})$ and $(t^{\text{II}}, x_2^{\text{II}})$ are the time and position of the first and second peaks (Fig. 4(c)) reaching a threshold gradient $\partial x_3/\partial x_2 =$ 0.06 (Fig. 4(a)) respectively. It has been theorized that the growth of the buckling amplitude follows the kinetic law $A(t) = A(0)e^{Et}$, where the coefficient E in the exponent captures the viscoelastic

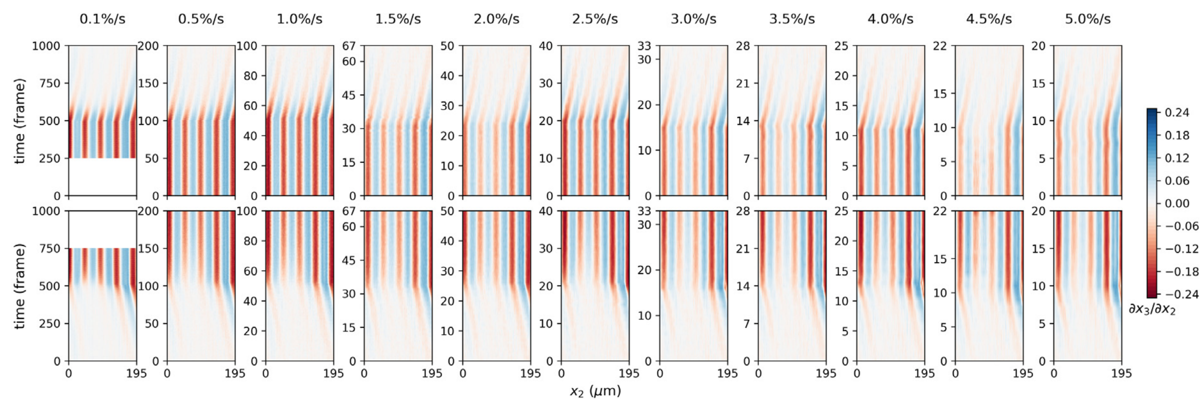

Fig. 3. Evolution of the centerline gradient at different strain rates. Top row: unbuckling in a modulated time window; Bottom row: buckling in a modulated time window; In all sub-figures, the frame rate is 100 frames per second.

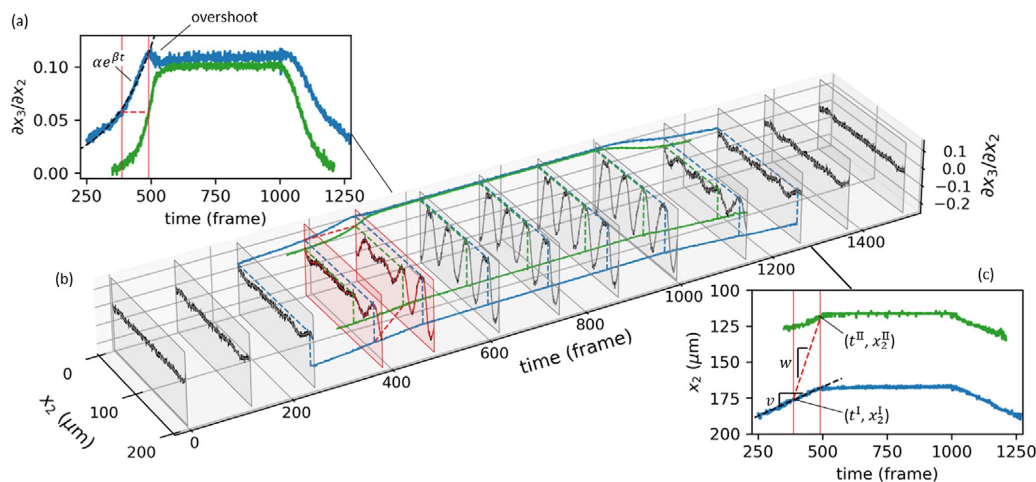

Fig. 4. In situ characterization of Si microribbon during buckling and unbuclking at strain rate 0.1%/s. The frame rate is 100 frames per second. (b) Evolution of the centerline, and the evolution of the firstly (blue) and secondly (green) formed positive gradient peaks projected in (a) the time — $\partial x_3/\partial x_2$ plane and (c) the time — x_2 plane. (For interpretation of the references to color in this figure legend, the reader is referred to the web version of this article.)

effect in the elastomer. [30,31] Here, we also use the exponential function $\alpha e^{\beta t}$ to fit the first gradient peak's growth curve (Fig. 4(a)). Fig. 5 plots the buckling speed v, the propagation speed w and the fitting parameters α and β at various strain rates. The error bars for v comes from changing the data range of linear fitting. The error bars for w are the result of mildly alternating the threshold gradient. Both speeds scale linearly with respect to the strain rate, especially in the low strain rate regime. The scaling coefficient for w is roughly 5 times as that for v. The fitted value of α is mostly insensitive to the strain rate, while the growth rate parameter β scales linearly with the strain rate. Our result is among the seldom experimentally measured value of the growth rate coefficient. Besides, although our exponential fitting function is inspired from viscoelasticity models [30,31], the linearity between β and the strain rate suggests that the elastic response dominates in our experiments.

It is widely accepted that buckling is the result of a bifurcation transition.[32–34] That is the system hops instantaneously from a metastable state to an admissible stable state in the energy landscape. However, the captured characteristic propagation in Si thin film reveals that the flat state and the fully buckled state are bridged by a sequence of partially buckled states. To confirm that those partially buckled configurations are also stable in a process of buckling, we captured the partially buckled states as holding the displacement for a prolonged period. The centerline gradient is indeed stabilized at a partially buckled state under various strain rates as shown in Fig. 6. The theory behind this physical phenomenon has not been established in the literature. We conjecture that the spatial heterogeneity in the viscoelastic substrate is responsible for the partially buckled stable state under the displacement control. We observed that the longitudinal propagation always occurs along the same spatial trajectory in all conducted experiments. In addition, the unequally evolved gradient peaks in Fig. 3 have the same spatial distribution under different strain rates. Our experiments suggest that the existing dynamics models should consider the strain heterogeneity for the thin film buckling on the soft substrate.

Functional fatigue caused by the debonding between thin film and soft substrate plays an important role in the fabrication and post-fabricated dynamics of stretchable MEMS. In order to study the fatigue and evolution of defects, we debond Si film and PDMS at two small regions and conduct 15 consecutive buckling/unbuckling cycles with 2% prestretch at strain rate 0.5% per second. From the supplementary movie S3, we observe that the buckled structure localized at the debonding regions, and the defects grow as the number of cycles increasing.

4. Conclusion

In summary, D-DInM is a useful tool to investigate thin film deflection quantitatively and in real-time at sub-micron to millimeter length scale. In this Letter, we found: (i) the major

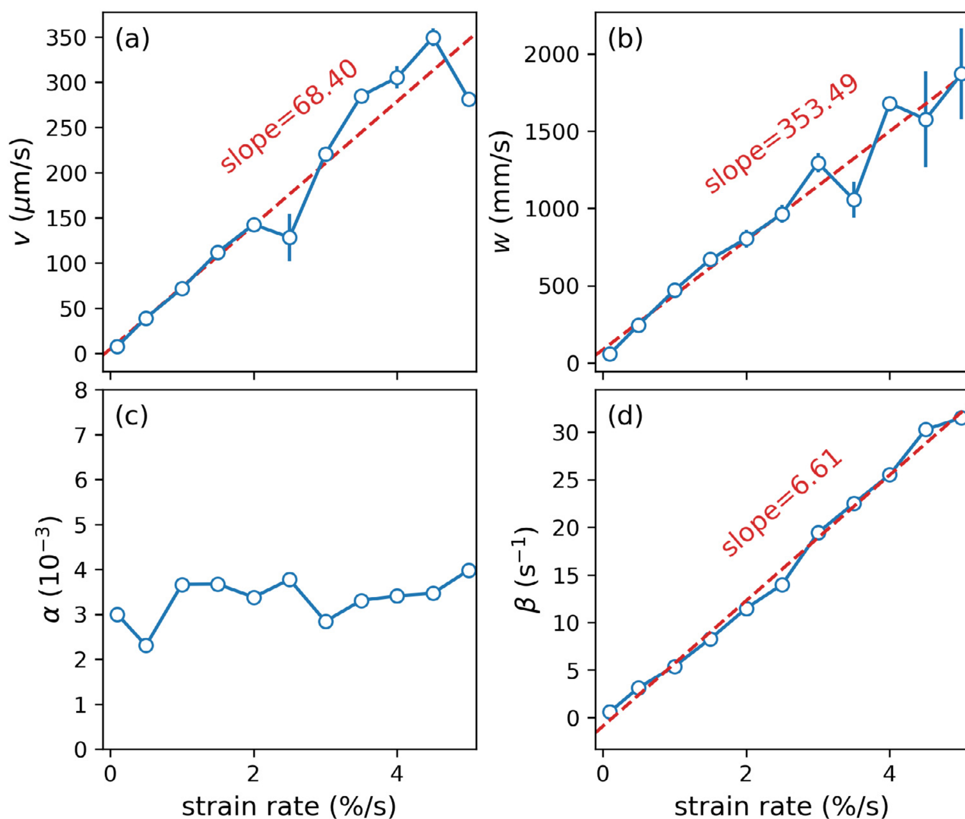

Fig. 5. Strain rate dependency of (a) the buckling speed, (b) the propagation speed, the fitting parameters of the gradient peak's growth curve: (c) α and (d) β.

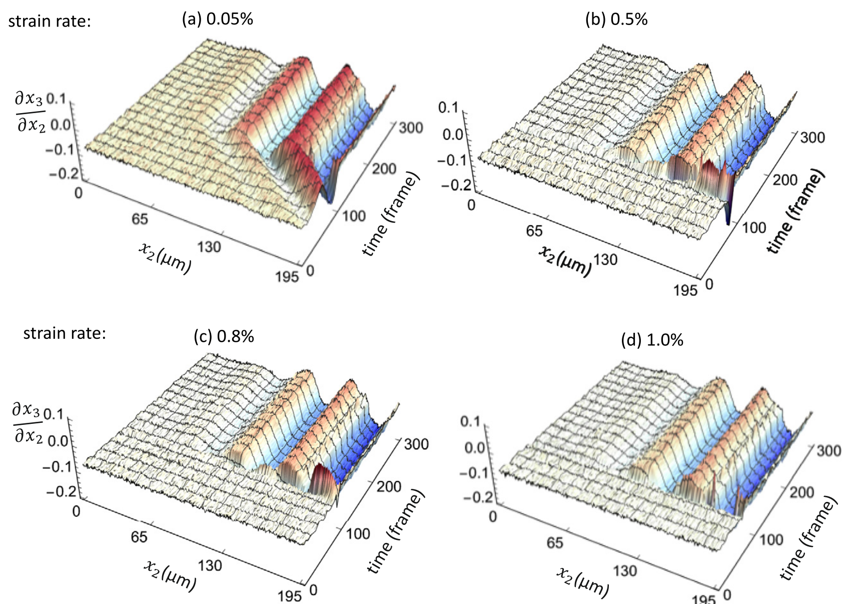

Fig. 6. Evolution of the centerline gradient from flat configuration to a partially buckled but stable configuration at strain rates of (a) 0.05% and (b) 0.5%, (c) 0.8% and (d) 1.0%.

features of the stabilized buckled structure are independent of strain rate between 0.1 and 5.0%/s; (ii) the buckled hills and valleys do not appear/disappear synchronously during the buckling/unbuckling process. Instead, the buckled/flat region propagates at a finite speed; (iii) during buckling, the buckled structure is pined at certain location and released after accumulating more contraction; (iv) the growth curve of the gradient peak fits well to an exponential formula, and the coefficient in the exponent is experimentally measured, which scales linearly with the strain rate; (v) both the buckling speed and the propagation speed are proportional to the strain rate, while the latter is much faster than the former. We conjecture that the local defects and the spatial heterogeneity of the substrate and the film are responsible for the longitudinal propagation during buckling. Only with real-time topography characterization for a large field of view, would one be able to capture such growth and propagation phenomena. The

dynamics of buckling and other surface deformation is crucial for soft electronic devices, not only for the fabrication stage but also for the post-deployment usage. Several observations presented in this paper cannot be fully explained by any of the existing models [20,30–33]. This work opens a new experimental scheme and provides new evidence for the theoretical study in this field.

Declaration of competing interest

The authors declare that they have no known competing financial interests or personal relationships that could have appeared to influence the work reported in this paper.

Acknowledgments

Z. Z. and X. C. acknowledge the financial support by the HK Research Grant Council, Hong Kong through grant no. 16201118 and the Collaborative Research Fund through grant no. C6016-20G.

Appendix A. Supplementary data

Supplementary material related to this article can be found online at https://doi.org/10.1016/j.eml.2021.101397.

References

[1] J. Yan, Y. Ma, X. Li, C. Zhang, M. Cao, W. Chen, S. Luo, M. Zhu, Y. Gao, Flexible and high-sensitivity piezoresistive sensor based on MXene composite with wrinkle structure, Ceram. Int. (2020).
[2] S. Choi, S. Lee, B. Lee, T. Kim, Y. Hong, Selective crack formation on stretchable silver nano-particle based thin films for customized and integrated strain-sensing system, Thin Solid Films (2020) 138068.
[3] H. Xu, Y.F. Lu, J.X. Xiang, M.K. Zhang, Y.J. Zhao, Z.Y. Xie, Z.Z. Gu, A multifunctional wearable sensor based on a graphene/inverse opal cellulose film for simultaneous, in situ monitoring of human motion and sweat, Nanoscale 10 (4) (2018) 2090–2098.
[4] M. Watanabe, H. Shirai, T. Hirai, Wrinkled polypyrrole electrode for electroactive polymer actuators, J. Appl. Phys. 92 (8) (2002) 4631–4637.
[5] D. De Tommasi, G. Puglisi, G. Saccomandi, G. Zurlo, Pull-in and wrinkling instabilities of electroactive dielectric actuators, J. Phys. D: Appl. Phys. 43 (32) (2010) 325501.
[6] J. Zhou, S.S. Sheiko, Reversible shape-shifting in polymeric materials, J. Polym. Sci. B 54 (14) (2016) 1365–1380.
[7] Z. Yan, M. Han, Y. Shi, A. Badea, Y. Yang, A. Kulkarni, E. Hanson, M.E. Kandel, X. Wen, F. Zhang, et al., Three-dimensional mesostructures as high-temperature growth templates, electronic cellular scaffolds, and self-propelled microrobots, Proc. Natl. Acad. Sci. 114 (45) (2017) E9455–E9464.
[8] S. Pellegrino, Deployable Structures, Vol. 412, Springer Science & Business Media, 2002.
[9] B. Tian, J. Liu, T. Dvir, L. Jin, J.H. Tsui, Q. Qing, Z. Suo, R. Langer, D.S. Kohane, C.M. Lieber, Macroporous nanowire nanoelectronic scaffolds for synthetic tissues, Nature Mater. 11 (11) (2012) 986–994.
[10] R. Feiner, L. Engel, S. Fleischer, M. Malki, I. Gal, A. Shapira, Y. Shacham-Diamand, T. Dvir, Engineered hybrid cardiac patches with multifunctional electronics for online monitoring and regulation of tissue function, Nature Mater. 15 (6) (2016) 679–685.
[11] F. Feng, X. Dang, R.D. James, P. Plucinsky, The designs and deformations of rigidly and flat-foldable origami, J. Mech. Phys. Solids (2020) 104018.
[12] J. Rogers, Y. Huang, O.G. Schmidt, D.H. Gracias, Origami mems and nems, MRS Bull. 41 (2) (2016) 123–129.
[13] C. Coupeau, J. Naud, F. Cleymand, P. Goudeau, J. Grilhé, Atomic force microscopy of in situ deformed nickel thin films, Thin Solid Films 353 (1–2) (1999) 194–200.
[14] P.J. Yoo, H.H. Lee, Evolution of a stress-driven pattern in thin bilayer films: Spinodal wrinkling, Phys. Rev. Lett. 91 (15) (2003) 154502.
[15] T. Ohzono, M. Shimomura, Ordering of microwrinkle patterns by compressive strain, Phys. Rev. B 69 (13) (2004) 132202.
[16] L. Ionov, Biomimetic 3D self-assembling biomicroconstructs by spontaneous deformation of thin polymer films, J. Mater. Chem. 22 (37) (2012) 19366–19375.
[17] W.M. Choi, J. Song, D.-Y. Khang, H. Jiang, Y.Y. Huang, J.A. Rogers, Biaxially stretchable "wavy" silicon nanomembranes, Nano Lett. 7 (2007) 1655–1663.
[18] T. Ohzono, H. Monobe, K. Shiokawa, M. Fujiwara, Y. Shimizu, Shaping liquid on a micrometre scale using microwrinkles as deformable open channel capillaries, Soft Matter 5 (23) (2009) 4658–4664.
[19] C.-M. Chen, J.C. Reed, S. Yang, Guided wrinkling in swollen, pre-patterned photoresist thin films with a crosslinking gradient, Soft Matter 9 (46) (2013) 11007–11013.
[20] H. Jiang, D.-Y. Khang, J. Song, Y. Sun, Y. Huang, J.A. Rogers, Finite deformation mechanics in buckled thin films on compliant supports, Proc. Natl. Acad. Sci. 104 (40) (2007) 15607–15612.
[21] S. Sasaki, S. Kidoaki, Precise design of microwrinkles through the independent regulation of elasticity on the surface and in the bulk of soft hydrogels, Polym. J. 52 (5) (2020) 515–522.
[22] M. Takahashi, T. Maeda, K. Uemura, J. Yao, Y. Tokuda, T. Yoko, H. Kaji, A. Marcelli, P. Innocenzi, Photoinduced formation of wrinkled microstructures with long-range order in thin oxide films, Adv. Mater. 19 (24) (2007) 4343–4346.
[23] K. Bashandeh, J. Lee, Q. Wu, Y. Li, X. Wang, Y. Shi, X. Guo, Y. Huang, J.A. Rogers, A.A. Polycarpou, Mechanics and deformatiotan of shape memory polymer kirigami microstructures, Extrem. Mech. Lett. (2020) 100831.
[24] C. Jin, B.C. Olsen, E.J. Luber, J.M. Buriak, Nanopatterning via solvent vapor annealing of block copolymer thin films, Chem. Mater. 29 (1) (2017) 176–188.
[25] K.A. Page, D.L. Patton, R. Huang, C.M. Stafford, Dynamics of confined polymer films measured via thermal wrinkling, Polym. Mater. Sci. Eng. 97 (2007) 784.
[26] Z. Zeng, C. Zhang, S. Du, X. Chen, Quantitative surface topography of martensitic microstructure by differential interference contrast microscopy, J. Mech. Phys. Solids 124 (2019) 102–114.
[27] Z. Zeng, H.-C. Chiu, L. Zhao, T. Zhao, C. Zhang, M. Karami, H. Yu, S. Du, X. Chen, Dual beam-shear differential interference microscopy for full-field surface deformation gradient characterization, J. Mech. Phys. Solids (2020) 104162.
[28] H.C. Chiu, Z. Zeng, L. Zhao, T. Zhao, S. Du, X. Chen, Measuring optical beam shear angle of polarizing prisms beyond the diffraction limit with localization method, Opt. Commun. 435 (2019) 227–231.
[29] D.-Y. Khang, H. Jiang, Y. Huang, J.A. Rogers, A stretchable form of single-crystal silicon for high-performance electronics on rubber substrates, Science 311 (5758) (2006) 208–212.
[30] N. Sridhar, D. Srolovitz, Z. Suo, Kinetics of buckling of a compressed film on a viscous substrate, Appl. Phys. Lett. 78 (17) (2001) 2482–2484.
[31] R. Huang, Kinetic wrinkling of an elastic film on a viscoelastic substrate, J. Mech. Phys. Solids 53 (1) (2005) 63–89.
[32] X. Chen, J.W. Hutchinson, Herringbone buckling patterns of compressed thin films on compliant substrates, J. Appl. Mech. 71 (5) (2004) 597–603.
[33] B. Audoly, A. Boudaoud, Buckling of a stiff film bound to a compliant substrate—Part i:: Formulation, linear stability of cylindrical patterns, secondary bifurcations, J. Mech. Phys. Solids 56 (7) (2008) 2401–2421.
[34] H.G. Allen, Analysis and Design of Structural Sandwich Panels: The Commonwealth and International Library: Structures and Solid Body Mechanics Division, Elsevier, 2013.